Progress In Electromagnetics Research Letter, Vol. 114, 13-19, 2023 PIER Letters

(Received 5 July 2023, Accepted 17 November 2023, Scheduled 25 November 2023)

Analysis of Long-Distance Propagation Characteristics of LF Multi-Hop Sky Waves

Lili Zhou[1, *], Xinyue Zhu[1], Zhonglin Mu[2], Yue Zheng[1], and Xinyue Hu[1]

[1] *The School of Electronic Information and Artificial Intelligence*
Shaanxi University of Science and Technology, Xi'an 710021, China
[2] *The Engineering Department, Air Force Engineering University, Xi'an 710038, China*

ABSTRACT: This paper focuses on the decomposition of different modes of Loran-C resultant waves, including ground waves and one-hop/two-hop sky waves, propagating in the Earth-ionosphere waveguide obtained from direct finite-difference time-domain (FDTD) modeling in the presence of the natural magnetic field. After providing the FDTD iterative formulas for the ionosphere affected by the natural magnetic field, the Loran-C resultant waves propagating in the anisotropic Earth-ionosphere waveguide are estimated using the FDTD algorithm. In both the daytime and nighttime ionosphere models, different orientations of the natural magnetic field are taken into account. The arrival times of the different propagation modes for the resultant waves were then determined using a multipath time-delay estimation method. With the above delays, the amplitudes of the different modes are acquired by solving overdetermined equations. Finally, the decomposition results are compared with those obtained in the absence of the natural magnetic field. The numerical experimental results indicate that, with a radiation power of 1 kW and a natural magnetic field of 0.5 Gs, the influence of the direction of the natural magnetic field on the field strength of one-hop sky waves is significant when the propagation distance of LF radio waves is less than 1000 km. Radio waves have multipath effects such as convergence, divergence, and diffraction due to the curvature of the Earth and the ionosphere. This results in significant interference phenomena when the propagation distance of two-hop sky waves is greater than 500 km.

1. INTRODUCTION

Low frequency (LF, 30–300 kHz) radio waves can propagate in the spherical shell waveguide formed by the Earth' surface and the conductive ionosphere, with the advantages of low attenuation and long propagation distances. At present, radio waves are widely used in many fields, such as remote communication systems, navigation, earthquake precursor detection, and geological exploration [1–3]. Due to the diverse propagation modes of radio waves, the propagation process is easily affected by propagation channels such as the Earth' surface, air, and ionosphere; thus the propagation characteristics are difficult to predict accurately. The large prediction error has become a bottleneck for improving the accuracy and upgrading the service of such systems.

Affected by the solar radiation, the parameters [4–6] such as electron density and collision frequency in the ionosphere will change periodically, resulting in regular daily and seasonal variations of the radio-wave propagation characteristics in the Earth-ionosphere waveguide [7, 8]. Compared with the traditional waveguide mode and wave-hop theories [9, 10], the finite-difference time-domain (FDTD) method can simulate the special Earth-ionosphere waveguide model with non-ideal boundaries, so as to consider continuous variations of radiopath parameters (electronic density, electron-neutral collision frequency, natural magnetic induction, topography, etc.) [11]. In 1999, Thèvenot et al. developed a two-dimensional (2-D) spherical-coordinate FDTD scheme for the calculation of VLF-LF propagation in the anisotropic Earth-ionosphere waveguide [12]. In 2000, Cummer reported another Earth-ionosphere waveguide model based on 2-D cylindrical coordinate FDTD, and analyzed the propagation of lightning radiation below 30 kHz [13]. In the follow-up study, Bérenger and Hu et al. further improved the accuracy of the model (e.g., by considering for more charged particles/Earth curvature) and introduced a moving computational domain, an implicit scheme and an correction of the angular dispersion to optimize the FDTD iteration strategy and reduce the computational costs [6, 14–16]. Around the same period, a global 3-D model [17–19] was developed by Simpson et al. In the above FDTD results, only the coupling characteristics of various modes in the Earth-ionosphere waveguide were studied, and no special distinction was made between ground-wave and sky-wave modes. Due to the interference effect, the characterization complexity of multipath coupled fields is far greater than that of single mode fields. Since 2011, we have studied the propagation characteristics of different mode waves in complex Earth-ionosphere waveguide based on the 2-D cylindrical-coordinate FDTD and parabolic equation methods. However, our study did not take into account the effects of the anisotropic ionosphere influenced by the natural magnetic field, and it was limited to the near-illumination region of one-hop sky waves [20–23].

---

* Corresponding author: Lili Zhou (zhoulili@sust.edu.cn).

doi:10.2528/PIERL23070502

2. FDTD ITERATIVE EQUATIONS IN THE PRESENCE OF THE NATURAL MAGNETIC FIELD

2.1. FDTD Model of LF Radio-Wave Propagation

The FDTD method is used to build a 2-D model (spherical shell form) for the long-distance propagation of LF radio waves in the Earth-ionosphere waveguide, with the radius of the Earth assumed to be 6370 km, as shown in Fig. 1.

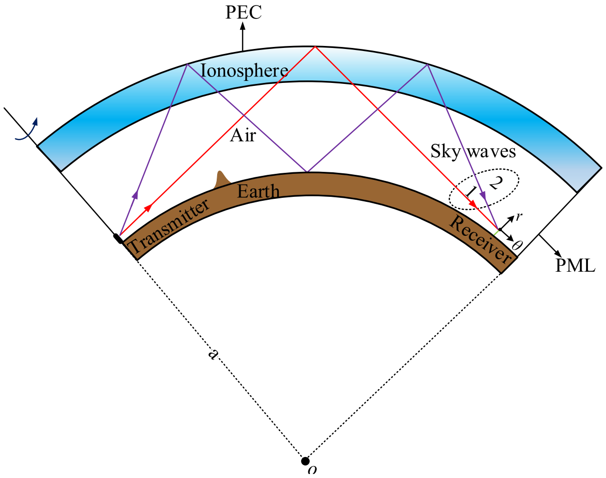

FIGURE 1. FDTD model of LF radio-wave propagation.

The FDTD computational domain is divided into ionosphere, air (free space), and ground layers from top to bottom. The symmetry axis serves as the left boundary of the computational domain. The transmitting antenna is positioned on the Earth's surface along the symmetry axis. Due to its long wavelength, it is equivalent to a vertical electric dipole. A perfect electric conductor (PEC) boundary is constructed at the upper boundary of the ionosphere and the lower boundary of the surface layer in the computational domain, while a perfect matching layer (PML) boundary is established on the right side, taking into account the absorption loss impact of the boundary. The specific meshing of the computational domain is shown in Fig. 2, the horizontal and vertical space steps are equivalent to $d\theta$ set to 6×10^{-6} rad and dr set to 37.5 m. The time step Δt is set to 31.25 ns. The electric field $\vec{E}$ and magnetic field $\vec{H}$ are decomposed into six components, namely E_r, E_θ, E_φ, H_r, H_θ, and H_φ. When LF radio waves are transmitted through the medium, current density $\vec{J}$ is formed due to the presence of numerous electrons and ions in the actual ionosphere. In general, the $\vec{J}$ generated by ions is negligible. Therefore, the effect of $\vec{J}$ generated by electrons in the Earth-ionosphere waveguide should be considered when updating $\vec{E}$ of the stratosphere and ionosphere. Each $\vec{J}$ component is computed at the same node as its corresponding $\vec{E}$ component.

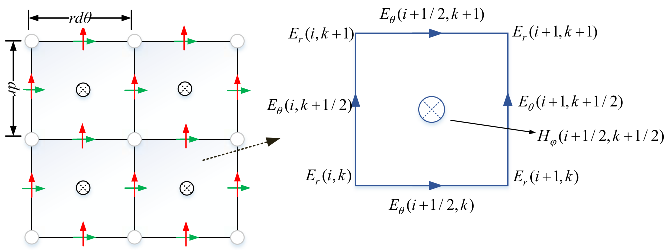

FIGURE 2. Mesh generation of FDTD.

2.2. Derivation of 2-D Cylindrical-Coordinate FDTD Equations in a Magnetized Plasma

This section emphasizes the iterative equations for the electromagnetic fields in an anisotropic ionosphere, where the ionosphere is modeled as a magnetized (cold) plasma. According to Maxwell equations, the fields satisfy [15]

$$\varepsilon_0 \frac{\partial \vec{E}}{\partial t} + \vec{J} = \nabla \times \vec{H} \tag{1}$$

$$\mu_0 \frac{\partial \vec{H}}{\partial t} = -\nabla \times \vec{E} \tag{2}$$

In the ionosphere, (1) and (2) are solved in parallel with an auxiliary equation that governs the current density [14]

$$\frac{d\vec{J}}{dt} + \frac{e}{m}\vec{J} \wedge \vec{B}_0 + \nu \vec{J} = \varepsilon_0 \omega_p^2 \vec{E} \tag{3}$$

with

$$\omega_p^2 = \frac{Ne^2}{m\varepsilon_0} \tag{4}$$

where e and m are the charge and mass of an electron; $\vec{B}_0$ is the natural magnetic field; N is the electron density; ν is the electron-neutral collision frequency; and ω_p is the plasma frequency.

The explicit FDTD scheme [12] is adopted, where the updating equations of $\vec{E}$ and $\vec{H}$ with time can be written in compact form as

$$\vec{E}^{n+1} = \vec{E}^{n} - \frac{\Delta t}{\varepsilon_0} \vec{J}^{n+1/2} + \frac{\Delta t}{\varepsilon_0} \nabla \times \vec{H}^{n+1/2} \tag{5}$$

where n represents the time step. The discretization details of $\vec{E}$ and $\vec{H}$ would not be repeated here. The equations for the advance of $\vec{J}$ are obtained by discretizing on time using the auxiliary Equation (1). To simplify the problem, the components of $\vec{J}$ are their averages over the time steps considered, thus obtaining

$$\begin{aligned} &\frac{\partial J_r}{\partial t} + \nu J_r + \frac{e}{m} \frac{J_\theta^{n-1/2} + J_\theta^{n+1/2}}{2} B_{0\varphi} \\ &- \frac{e}{m} \frac{J_\varphi^{n-1/2} + J_\varphi^{n+1/2}}{2} B_{0\theta} = \varepsilon_0 \omega_p^2 E_r^n \end{aligned} \tag{6}$$

$$\begin{aligned} &\frac{\partial J_\theta}{\partial t} + \nu J_\theta + \frac{e}{m} \frac{J_\varphi^{n-1/2} + J_\varphi^{n+1/2}}{2} B_{0r} \\ &- \frac{e}{m} \frac{J_r^{n-1/2} + J_r^{n+1/2}}{2} B_{0\varphi} = \varepsilon_0 \omega_p^2 E_\theta^n \end{aligned} \tag{7}$$

$$\frac{\partial J_\varphi}{\partial t} + \nu J_\varphi + \frac{e}{m} \frac{J_r^{n-1/2} + J_r^{n+1/2}}{2} B_{0\theta}$$

$$-\frac{e}{m}\frac{J_\theta^{n-1/2}+J_\theta^{n+1/2}}{2}B_{0r}=\varepsilon_0\omega_p^2E_\varphi^n \tag{8}$$

where J_r, J_θ, and J_φ are the components of the $\vec{J}$ in the r, θ, and φ directions, respectively. B_{0r}, $B_{0\theta}$, and $B_{0\varphi}$ are the components of $\vec{B_0}$. From (6)–(8), it can be seen that the three components of $\vec{J}$ are interrelated. With the semi-exponential difference method in [12], we can get the following matrix form

$$\mathbf{A}\mathbf{J}^{n+1/2}=\mathbf{B}\mathbf{J}^{n-1/2}+b\varepsilon_0\omega_p^2\mathbf{E}^n \tag{9}$$

where $\mathbf{A}=\begin{bmatrix}1 & b\omega_{b\varphi}/2 & -b\omega_{b\theta}/2\\ -b\omega_{b\varphi}/2 & 1 & b\omega_{br}/2\\ b\omega_{b\theta}/2 & -b\omega_{br}/2 & 1\end{bmatrix}$,

$\mathbf{B}=\begin{bmatrix}a & -b\omega_{b\varphi}/2 & b\omega_{b\theta}/2\\ b\omega_{b\varphi}/2 & a & -b\omega_{br}/2\\ -b\omega_{b\theta}/2 & b\omega_{b_r}/2 & a\end{bmatrix}$, $\mathbf{J}=\begin{bmatrix}J_r\\ J_\theta\\ J_\varphi\end{bmatrix}$,

and $\mathbf{E}=\begin{bmatrix}E_r\\ E_\theta\\ E_\varphi\end{bmatrix}$. The other variables are $a=\mathrm{e}^{-\nu\Delta t}$, $b=(1-\mathrm{e}^{-\nu\Delta t})/\nu$, $\omega_{b\theta}=\frac{e}{m}B_{0\theta}$, $\omega_{b\varphi}=\frac{e}{m}B_{0\varphi}$, and $\omega_{br}=\frac{e}{m}B_{0r}$. Equation (9) is further replaced by

$$\mathbf{J}^{n+1/2}=\mathbf{C}_1\mathbf{J}^{n-1/2}+b\varepsilon_0\omega_p^2\mathbf{C}_2\mathbf{E}^n \tag{10}$$

where $\mathbf{C}_1=\mathbf{A}^{-1}\mathbf{B}$ and $\mathbf{C}_2=\mathbf{A}^{-1}$. Here, taking the component J_r as an example, the equation for the advance of it at point $(i,k+1/2)$ of the mesh is

$$\begin{aligned}J_r^{n+1/2}(i,k+1/2)&=(\mathbf{C}_1)_{11}J_r^{n-1/2}(i,k+1/2)\\&+(\mathbf{C}_1)_{12}J_\theta^{n-1/2}(i,k+1/2)+(\mathbf{C}_1)_{13}J_\varphi^{n-1/2}(i,k+1/2)\\&+b\varepsilon_0\omega_p^2(\mathbf{C}_2)_{11}E_r^n(i,k+1/2)+b\varepsilon_0\omega_p^2(\mathbf{C}_2)_{12}\\&E_\theta^n(i,k+1/2)+b\varepsilon_0\omega_p^2(\mathbf{C}_2)_{13}E_\varphi^n(i,k+1/2)\end{aligned} \tag{11}$$

For the FDTD grid generation method shown in Figure 2, the nodes of some field quantities ($J_\theta^{n-1/2}(i,k+1/2)$, $J_\varphi^{n-1/2}(i,k+1/2)$, $E_\theta^n(i,k+1/2)$, and $E_\varphi^n(i,k+1/2)$) in (11) do not exist, and they should be obtained by averaging the surrounding field values.

2.3. Decomposition of Electromagnetic Waves with Different Modes

The above FDTD method is used to predict the Loran-C [24] resultant waves with multipropagation modes in the Earth-ionosphere waveguide in the presence of the natural magnetic field. The carrier frequency of Loran-C is 100 kHz and its excitation current is defined as [23]

$$\begin{aligned}i_s(t)&=A_0(t-\tau)^2\exp\left[-2(t-\tau)/6.5\times10^{-5}\right]\\&\sin\left(2\pi\times10^5t\right)\end{aligned} \tag{12}$$

where $\tau\le t\le\tau+6.5\times10^{-5}$, and $i_s(t)=0$ when $t\le\tau$. And A_0 is a constant.

The resultant field predicted by FDTD can be decoupled because it can be viewed as the superposition of multiple signals with the same waveform but different amplitudes and delays. How to obtain the amplitudes and delays of different model waves from the resultant signal is described in [23]. First, the time delays of different propagation modes in the resultant field can be obtained by using a multipath time delay estimation method (employing the combined FFT/IFFT spectral-division technique and filtering process). Subsequently, a set of overdetermined equations are further constructed to solve the amplitudes based on the obtained delay information. For example, supposing the arrival times of different modes in E_r are τ_0, τ_1 ..., and τ_m, and the corresponding amplitudes a_0, a_1 ..., and a_m of different modes can be solved by

$$\begin{bmatrix}E_r^n\\ E_r^{n-1}\\ \cdots\\ E_r^{n_0+1}\\ E_r^{n_0}\end{bmatrix}=\begin{bmatrix}E_0^{n-n_0} & E_0^{n-n_1} & \cdots & E_0^{n-n_m}\\ E_0^{n-1-n_0} & E_0^{n-1-n_1} & \cdots & E_0^{n-1-n_m}\\ \cdots & \cdots & \cdots & \cdots\\ E_0^1 & E_0^{n_0+1-n_1} & \cdots & E_0^{n_0+1-n_m}\\ E_0^0 & E_0^{n_0-n_1} & \cdots & E_0^{n_0-n_m}\end{bmatrix}\cdot\begin{bmatrix}a_0\\ a_1\\ \cdots\\ a_{m-1}\\ a_m\end{bmatrix} \tag{13}$$

where E_0^n denotes the standard Loran-C field [23] at the time step n, and $E_0^n=0$ if $n<0$. n_0, n_1 ..., and n_m denote the discrete time steps of τ_0, τ_1 ..., and τ_m.

3. SIMULATION ANALYSIS OF DIFFERENT MODELS

In this section, the Loran-C resultant waves propagating in different Earth-ionosphere waveguide models are predicted and decomposed. In addition, the results of the decomposed one-hop/two-hop sky waves are compared in ionospheric models with and without the natural magnetic field. All observation points are on the Earth's surface. Our numerical experiments use a radiated power of 1 kW and ground electrical parameters set at $\sigma=3\times10^{-3}$ S/m and $\varepsilon_r=13$. The ionosphere adopts the classical gradient model, where the electron density N (m^{-3}) and collision frequency ν (s^{-1}) are

$$N=1.43\times10^{13}\mathrm{e}^{-0.15h'}\mathrm{e}^{(\beta-0.15)(h-h')} \tag{14}$$

$$\nu=1.816\times10^{11}\mathrm{e}^{-0.15h} \tag{15}$$

where h is the altitude in km, and (β,h') equal (0.5, 87 km) and (0.3, 72 km) for nighttime and daytime, respectively. The natural magnetic fields B_0 with three different orientations are accounted for: horizontal, $B_{0\theta}=5\times10^{-5}$ T, $B_{0r}=B_{0\varphi}=0$ T; vertical, $B_{0r}=5\times10^{-5}$ T, $B_{0\theta}=B_{0\varphi}=0$ T; 45° (directed 45 degrees from the ground and the plane of the calculation), $B_{0\theta}=B_{0\varphi}=2.5\times10^{-5}$ T, $B_{0r}=5\times10^{-5}/\sqrt{2}$ T. And the natural magnetic field is constant along the whole radiopath.

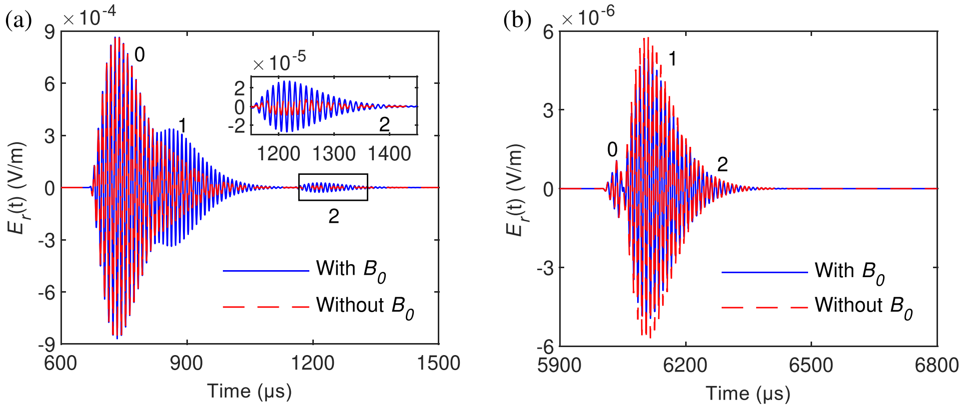

FIGURE 3. Resultant waves at different observation positions during daytime (B_0 orientation is 45°). (a) The observation point is 200 km. (b) The observation point is 1800 km.

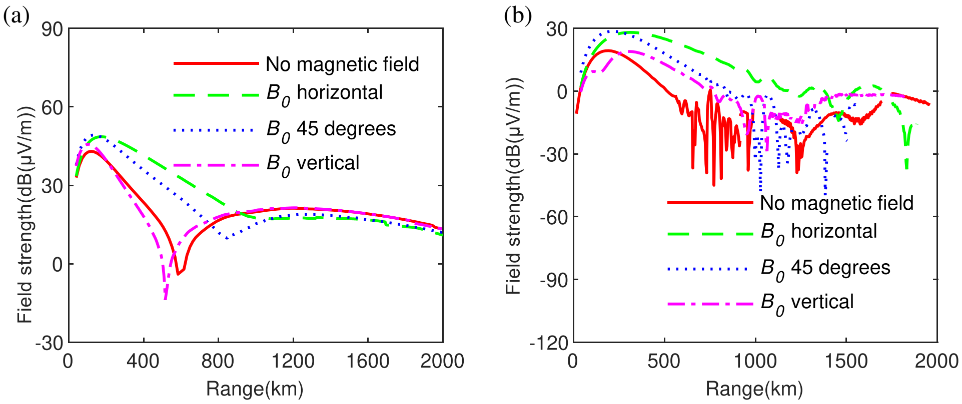

FIGURE 4. Influence of different orientation of B_0 on the field strength of LF one- and two-hop sky waves during daytime. (a) One-hop sky waves. (b) Two-hop sky waves.

3.1. Flat-Earth and Inhomogeneous-Ionosphere Model

This section mainly studies the decomposition of different modes in the Loran-C resultant waves where the ground is flat, and the ionosphere parameters gradually change. The maximum distance between the receiving point on the ground and the dipole source is set at 2000 km. The lower boundary of the ionosphere is set at an altitude 30 km in flat-earth and inhomogeneous-ionosphere model.

3.1.1. Simulation for the Daytime Profile

Figures 3 and 4 show a comparison of the results for the vertical electric field E_r in the presence and absence of the natural magnetic field in the ionosphere for the case where the ionosphere is daytime model parameters. The upper boundary of the ionosphere is located at an altitude 70 km above the Earth's surface. Figure 3 displays the resultant wave of the electric field E_r at observation points that are 200 km and 1800 km from the dipole source, respectively. Here, B_0 is oriented 45° from the ground and 45° from the plane of propagation, with a magnitude of 0.5 G. The different mode waves are labeled in it, where 0 represents the ground waves; 1 represents the one-hop sky waves; and 2 represents the two-hop sky waves. Figure 4 shows the variation of the decoupled one-hop sky-wave and part of two-hop sky-wave field strength with the propagation distance, and B_0 is taken in three different directions mentioned above.

As can be seen from Figure 3, when LF radio waves propagate to receiving points relatively close to the transmitter point, their ground-wave field values are significantly larger than sky waves. However, the attenuation rate of the ground-wave field during propagation is greater than that of the sky-wave field. Therefore, when LF radio waves propagate to a certain distance, the values of the sky-wave field become greater than those of the ground waves. This phenomenon indicates that the sky waves propagate farther compared with ground waves. From Figure 4, it can be observed that in the absence of the natural magnetic field, the field strength of one-hop sky waves reaches an extreme point, around 600 km from the receiving point. When the influence of B_0 is present, the position of the extreme point changes with the different directions of B_0. The greater the angle of B_0 from the ground and the plane is, the closer the position of the extreme point is to the position of the transmitting antenna. This phenomenon occurs due to changes in the propagation distance of LF radio waves cause changes in the incidence angle of radio waves. When combined with the effect of the Earth's curvature, it leads to complex changes in the reflection coefficient of the ionosphere. It is noteworthy that, unlike the one-hop sky-wave field, the two-hop sky-wave

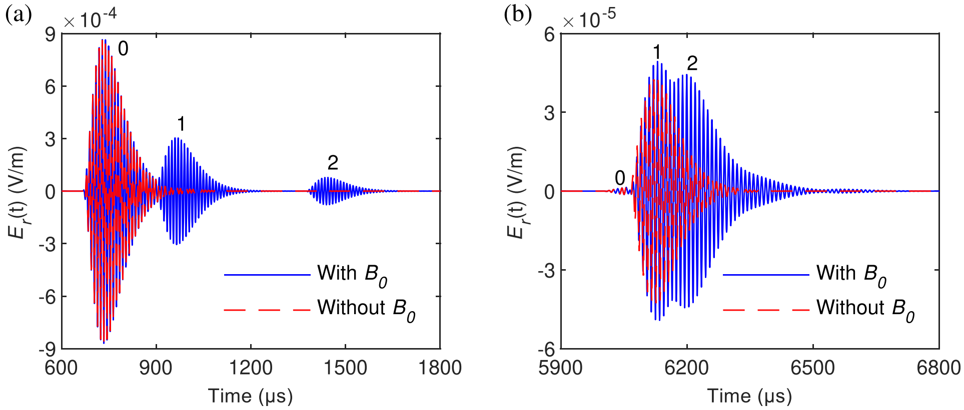

FIGURE 5. Resultant waves at different observation positions during nighttime (B_0 orientation is 45°). (a) The observation point is 200 km. (b) The observation point is 1800 km.

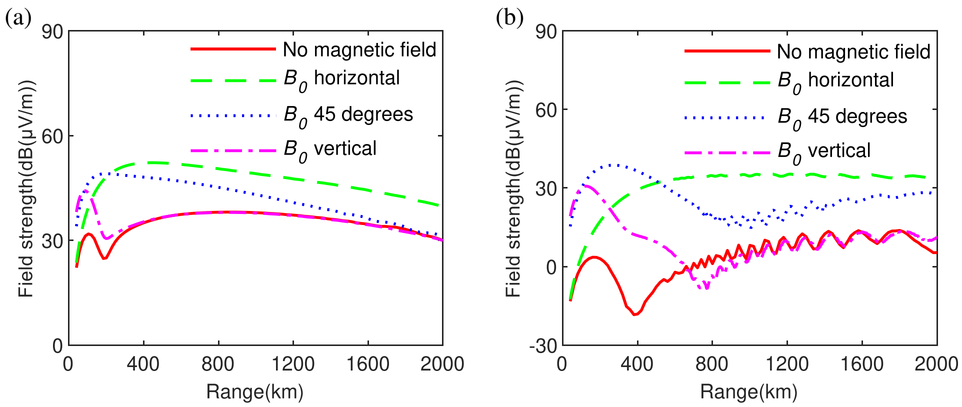

FIGURE 6. Influence of different orientation of B_0 on the field strength of LF one- and two-hop sky waves during nighttime. (a) One-hop sky waves. (b) Two-hop sky waves.

field has a clear interference phenomenon at a distance 500 km from the source point. Even without the influence of B_0, the interference phenomenon still exists. The analysis shows that the interference phenomenon is mainly caused by the multipath factors such as convergence, divergence and diffraction of radio waves caused by the curvature of the ionosphere and the Earth. Since the attenuation of two-hop sky waves is significantly greater than that of one-hop sky waves, and the field strength of two-hop sky waves at the same receiving point is much smaller than that of one-hop sky waves, the algorithm in this paper is difficult to detect in some areas and there is a certain error in the detection process at longer distances. Therefore, we only provide the distribution of the two-hop sky-wave field at detectable locations in Figure 4(b). The above results suggest that B_0 has a minor impact on the field strength of LF one-hop sky waves propagating over long distances during the daytime.

3.1.2. Simulation for the Nighttime Profile

Figures 5 and 6 show a comparison of the results for E_r in the presence and absence of the natural magnetic field in the ionosphere, considering nighttime model parameters for the ionosphere. The upper boundary of the ionosphere is 90 km above the ground. The results given in Figure 5 represent the resultant wave of the electric field E_r, with the location of the observation points and the orientation of B_0 remaining the same as in Figure 3. One-hop/two-hop sky-wave and ground-wave modes are labeled in this figure. Figure 6 shows the variation the field strength of the decoupled one-hop sky waves and two-hop sky waves with the propagation distance, and B_0 is taken in three different directions mentioned above.

From Figure 5, it can be seen that the ground-wave field is the largest at the 200 km receiving point, and the one-hop sky-wave field with the influence of B_0 is significantly greater than that without the influence of B_0. Additionally, the one-hop sky-wave field is most pronounced at the 1800 km receiving point, while two-hop sky-wave field is most significantly affected by B_0. Comparing Figure 6 with Figure 4, it can be seen that the effect of B_0 on the field strength of the Roland-C signal is more significant during nighttime than during daytime. Moreover, the field strength trends of different modes of sky waves are also complicated under the effect of B_0 in different directions. The polarization conversion effect is more pronounced at night due to the influence of B_0, resulting in a significant change of sky-wave field values. In the nighttime model, the variation trend of the one-hop sky-wave field strength is slower for one-hop sky waves when the receiving point is farther from the dipole source

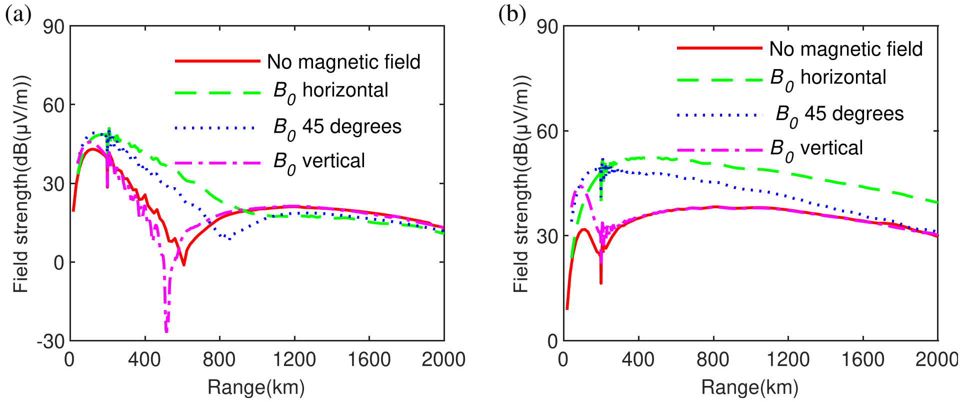

FIGURE 7. Field strength variations of one-hop sky waves along the irregular ground for different orientations of B_0. (a) Daytime. (b) Nighttime.

location than for those closer. Figure 5 shows that the two-hop sky-wave field has obvious interference when the propagation distance exceeds 700 km, especially when the orientation of B_0 is vertical. In comparison with the long-distance results in the daytime model, the algorithm detects better due to the higher ionospheric height at night and the larger field strength of two-hop sky waves during the nighttime.

3.2. Irregular-Earth and Inhomogeneous-Ionosphere Model

Figure 7 illustrates the effect of three different orientations of B_0 on the field strength variations of one-hop sky waves propagating in complex Earth-ionosphere waveguide characterized by irregular topography and asymptotic ionospheric parameters. In Figure 7(a), the ionosphere in the model adopts the daytime parameters mentioned above, while nighttime ionospheric parameters mentioned above are utilized in Figure 7(b). The orientations of the natural magnetic field and the ionospheric altitude above the ground in both models shown in Figure 7 is consistent with the daytime and nighttime models mentioned above. Additionally, there is a Gaussian-shaped mountain (1.5 km high and 10 km wide) on the ground 200 km from the dipole source with an average slope of about [21].

It can be seen from Figure 7 that, compared with the flat-Earth model, the mountain renders the characteristics of one-hop sky-wave field strength more complex. In the irregular-Earth and inhomogeneous-ionosphere waveguide, the variation trends of one-hop sky waves close to the mountain regions are no longer gentle but change dramatically with the topographic relief. Even in the flat regions in front and behind mountains, extracting sky-wave modes with two hops using FFT/IFFT spectral division method, as in the flat-Earth model, becomes challenging. Due to the increased multipath interference caused by scattered and reflected waves from the mountain, the propagation characteristics of different wave-hop sky waves received on the ground become significantly complex. In addition, consistent with the above conclusion, the natural magnetic field has a more pronounced impact on the radio-wave propagation characteristics at night when the upper PEC boundary is placed at 90 km from the Earth's surface.

4. CONCLUSION

Based on a series of FDTD numerical experiments, LF resultant waves in the anisotropic Earth-ionosphere waveguide are computed, and the characteristics of one-hop and two-hop sky waves are obtained by decomposing the predicted skywave modes of Loran-C signals. The FDTD models in this paper not only consider the ground irregularity and diurnal variation of ionosphere parameters, but also take the influence of natural magnetic field into account. By reducing the interference between different modes, the complexity of characterizing LF sky waves is somewhat reduced, which is beneficial for expanding the application of LF sky waves. Because the ionosphere in the real environment is susceptible to the influence of many factors, the variation patterns of sky waves will be more complicated. Therefore, how to obtain the variation patterns of sky waves under complex ionospheric conditions is the next important research work.

ACKNOWLEDGEMENT

This work was supported by the National Natural Science Foundation of China (No. 62171265).

REFERENCES

[1] Pu, Y., H. Yang, L. Wang, Y. Zhao, R. Luo, and X. Xi, "Analysis and modeling of temporal variation properties for LF ground-wave propagation delay," *IEEE Antennas Wireless Propagat. Lett.*, Vol. 18, No. 4, 641–645, 2019.

[2] Chen, C. H., L. Lin, T. Yeh, S. Wen, H. Yu, C. Yu, Y. Gao, P. Han, Y. Y. Sun, J. Y. Liu, C. H. Lin, C. C. Yang, C. M. Lin, H. H. Hsieh, and P. J. Lu, "Determination of epicenters before earthquakes utilizing far seismic and GNSS data: Insights from ground vibrations," *Remote Sens.*, Vol. 12, No. 19, 3252, 2020.

[3] Qiu, L., Z. Yang, E. Wang, and B. Li, "Early-warning of rock burst in coal mine by low-frequency electromagnetic radiation," *Eng. Geol.*, 2020.

[4] Niknan, K. and J. J. Simpson, "A review of grid-based, time-domain modeling of electromagnetic wave propagation involving the ionosphere," *IEEE J. Multiscale Multiphys. Comput. Techn.*, Vol. 6, 214–228, 2021.

[5] Nina, A., "Modelling of the electron density and total electron content in the quiet and solar X-ray flare perturbed ionospheric d-region based on remote sensing by VLF/LF signals," *Remote Sens.*, Vol. 14, No. 1, 2021.

[6] Bérenger, J. P., "FDTD propagation of VLF-LF waves in the presence of ions in the Earth-ionosphere waveguide," *Ann. Telecommun.*, Vol. 75, No. 18, 437–446, 2020.

[7] Gu, T., L. Xu, and K. Li, "Mode interferences of VLF waves in an anisotropic waveguide due to sunrise and sunset," *IEEE Trans. Antennas Propag.*, Vol. 66, No. 12, 7255–7264, 2018.

[8] Wang, J. C. H., "Seasonal variation of LF/MF sky-wave field strengths," *IEEE Trans. Broadcast.*, Vol. 54, No. 3, 437–440, 2008.

[9] Wakai, N., N. Kurihara, and A. Otsuka, "Numerical method for calculating LF sky-wave, ground-wave and their resultant wave field strengths," *Electron. Lett.*, Vol. 40, No. 5, 288–290, 2004.

[10] Xu, H., T. Gu, and J. Zhang, "LF skywave propagation excited by a horizontal electric dipole towards understanding of its radiation mechanism," *Appl. Comput. Electrom.*, Vol. 33, No. 6, 657–664, 2018.

[11] Bérenger, J. P., "FDTD computation of VLF-LF propagation in the Earth-ionosphere waveguide," *Ann. of Télécommun.*, Vol. 57, Nos. 11–12, 1059–1090, 2002.

[12] Thevenot, M., J. P. Bérenger, T. Monediere, and F. Jecko, "A FDTD scheme for the computation of VLF-LF propagation in the anisotropic Earth-ionosphere waveguide," *Ann. Telecommun.*, Vol. 54, Nos. 5–6, 297–310, 1999.

[13] Cummer, S. A., "Modeling electromagnetic propagation in the Earth-ionosphere waveguide," *IEEE Trans. Antennas Propag.*, Vol. 48, No. 9, 1420–1429, 2000.

[14] Bérenger, J. P., "Long range propagation of lightning pulses using the FDTD method," *IEEE Trans. Electromagn. Compat.*, Vol. 47, No. 4, 1008–1011, 2005.

[15] Bérenger, J. P., "An implicit FDTD scheme for the propagation of VLF-LF radio waves in the Earth-ionosphere waveguide," *C. R. Phys.*, Vol. 15, 393–402, 2014.

[16] Hu, W. Y. and S. A. Cummer, "An FDTD model for low and high altitude lightning-generated EM fields," *IEEE Trans. Antennas Propag.*, Vol. 54, No. 5, 1513–1522, 2006.

[17] Simpson, J. J. and A. Taflove, "A review of progress in FDTD Maxwell's equations modeling of impulsive subionospheric propagation below 300 kHz," *IEEE Trans. Antennas Propag.*, Vol. 55, No. 6, 1582–1590, 2007.

[18] Yu, Y. X. and J. J. Simpson, "An E-J collocated 3-D FDTD model of electromagnetic wave propagation in magnetized cold plasma," *IEEE Trans. Antennas Propag.*, Vol. 58, No. 2, 469–478, 2009.

[19] Pokhrel, S., V. Shankar, and J. J. Simpson, "3-D FDTD modeling of electromagnetic wave propagation in magnetized plasma requiring singular updates to the current density equation," *IEEE Trans. Antennas Propag.*, Vol. 66, No. 9, 4772–4781, 2018.

[20] Zhou, L., J. Yan, Z. Mu, Y. Pu, Q. Wang, and L. He, "Field-strength variations of LF one-hop sky waves propagation in the Earth-ionosphere waveguide at short ranges," *IEEE Antennas Wireless Propag. Lett.*, Vol. 18, No. 9, 1780–1783, 2019.

[21] Zhou, L., X. Xi, J. Liu, and N. Yu, "LF ground-wave propagation over irregular terrain," *IEEE Trans. Antennas Propag.*, Vol. 59, No. 4, 1254–1260, 2011.

[22] Zhou, L., Y. Jiang, Z. Mu, Q. Wang, X. Hu, and L. He, "Study of Loran-C one-hop sky-wave fields at different altitudes above the ground," *IEEE Antennas Wireless Propagat. Lett.*, Vol. 20, No. 12, 2368–2371, 2021.

[23] Zhou, L., Q. Wang, Z. Mu, J. Yan, J. Zhu, and L. He, "Decomposition of LF resultant waves with multi-propagation modes in the Earth-ionosphere waveguide," *IEEE Trans. Antennas Propag.*, Vol. 69, No. 6, 2368–2371, 2021.

[24] Wang, K. S. Tang, J. Ke, and Y. Hou, "A small active magnetic antenna of Loran-C," *IEEE Sens. J.*, Vol. 23, No. 1, 647–657, 2022.